Detonation shock dynamics and comparisons with direct numerical simulation

Tariq D. Aslam*, and D. Scott Stewart†

August 17, 1998

Abstract

Comparisons between direct numerical simulation (DNS) of detonation and detonation shock dynamics (DSD) is made. The theory of DSD defines the motion of the detonation shock in terms of intrinsic geometry of the shock surface, in particular for condensed phase explosives the shock normal velocity, D_n, the normal acceleration, $\dot{D}_n$, and the total curvature, κ. In particular, the properties of three intrinsic front evolution laws are studied and compared. These are 1) Constant speed detonation (Huygens' construction), 2) Curvature dependent speed propagation ($D_n - \kappa$ relation), and 3) Curvature and speed dependent acceleration ($\dot{D}_n - D_n - \kappa$ relation). We show that it is possible to measure shock dynamics directly from simulation of the reactive Euler equations and that subsequent numerical solution of the intrinsic partial differential equation for the shock motion (e.g. a $\dot{D}_n - D_n - \kappa$ relation) reproduces the computed shock motion with high precision.

*Corresponding Author, Los Alamos National Laboratory, Los Alamos, NM 87545
†University of Illinois , Urbana, IL 61801

1 Introduction

For nearly a century, the steady, one-dimensional Chapman–Jouget velocity, D_{CJ} [1], [2] has been used as a coarse prediction of experimental observations. For nearly as long, engineers have used the steady, one-dimensional results to predict the motion of unsteady, multi-dimensional detonation shock fronts. The rule that a detonation front propagates at a constant speed in a direction normal to itself is equivalent to a Huygens' construction. Although this model for detonation front motion is simple, it does not predict many aspects of multi-dimensional detonation flows. For example, detonation velocities have been observed to change by as much as 40% due to multi-dimensional effects [3]. Failure of detonation waves has also been observed experimentally. Other dynamics, such as pulsating and cellular detonations, can not be predicted by such a simple propagation rule.

Detonation shock dynamics (DSD) [4] [13] [14] [12] is an asymptotic theory whose key result is an intrinsic partial differential equation (PDE) for the dynamics of the detonation shock front. The theory of DSD defines the motion of the detonation shock in terms of the intrinsic geometry of the shock surface, in particular for condensed phase explosives the shock normal velocity, D_n, the normal acceleration, $\dot{D}_n$, and the total curvature, κ [12]. The engineering method of DSD does not solve the reactive Euler equations, but rather it solves the intrinsic PDE, subject to appropriate boundary and initial conditions, associated with a particular explosive system. See [6] for a discussion of appropriate angle boundary conditions for DSD. The solution can be coupled with equation of state information to calculate shock pressures and other pertinent information. Thus it is critical to determine the intrinsic PDE whose solution can reproduce the motion of the detonation shock. It will be demonstrated that DSD front propagation models can predict several aspects of unsteady multi-dimensional detonations accurately.

Once an appropriate relation for a particular explosive system is determined, the ability to predict the resulting initial-boundary-value problem for the evolution of the detonation shock front is needed. The numerical solution of the resulting intrinsic DSD PDEs can be integrated analytically for problems with special geometries, such as planar, cylindrical and spherical problems. Even then, it is not always possible to get a solution in closed form. Typical engineering applications involve very complicated boundaries, and the front can experience such topological changes as merging and burn-

ing out. Thus, the focus of this paper will be the numerical solutions of these intrinsic DSD PDEs subject boundary and initial data and verification of DSD models by comparison with direct numerical simulation (DNS) of multi-dimensional unsteady detonation problems. We will focus on two DSD relations, a $D_n - \kappa$ relation and a $\dot{D}_n - D_n - \kappa$ relation.

2 Reactive Euler equations and direct numerical simulation

Here, comparisons between DSD and direct numerical simulations of detonation are made. The simulations were carried out with a code described in [10]. The code is based on a high-order Godunov-type shock-capturing scheme. Of particular interest is the dynamics of the detonation front. In Section 2.1, the mathematical formulation of the detonation model used in the DNS is presented.

Since DSD is an asymptotic theory, one would like to establish how well it predicts shock front evolution. One way of accomplishing this goal is to compare a DSD solution to a high resolution solution of a multi-dimensional detonation problem via a resolved numerical simulation of the reactive, compressible Euler equations.

An algorithm for solving the compressible reactive Euler equations is outlined. Then, comparisons of the dynamics of the shock front from DSD models to the resolved DNS are made.

2.1 Reactive Euler equations

The reactive Euler equations express conservation of mass, momentum, and energy and include a reaction rate law as follows:

$$\begin{aligned}
\frac{D\rho}{Dt} + \rho\vec{\nabla}\cdot\vec{u} = 0 \quad , \\
\rho\frac{D\vec{u}}{Dt} + \vec{\nabla}p = 0 \quad , \\
\frac{De}{Dt} + p\frac{D(1/\rho)}{Dt} = 0 \quad , \\
\frac{D\lambda}{Dt} = r(p,\rho,\lambda) \quad , \qquad (1)
\end{aligned}$$

For purpose of illustration, the polytropic equation of state (EOS) is used,

$$e = \frac{p}{\rho(\gamma-1)} - Q\lambda \quad ,$$

where Q is the heat of detonation, λ is the reaction progress variable ($\lambda = 0$ for unreacted material, and $\lambda = 1$ for completely reacted material). The reaction rate is r.

Written in conservative form, in 2-D Cartesian coordinates, these become:

$$
\begin{aligned}
(\rho)_t + (\rho u)_x + (\rho v)_y &= 0 \quad , \\
(\rho u)_t + (\rho u^2 + p)_x + (\rho uv)_y &= 0 \quad , \\
(\rho v)_t + (\rho uv)_x + (\rho v^2 + p)_y &= 0 \quad , \\
(E)_t + (uE + up)_x + (vE + vp)_y &= 0 \quad , \\
(\rho\lambda)_t + (\rho u\lambda)_x + (\rho v\lambda)_y &= \rho r(p, \rho, \lambda)
\end{aligned} \tag{2}
$$

where

$$E = \rho e + \frac{\rho}{2}(u^2 + v^2)$$

is the total energy. Next, a numerical method will be presented that is used to solve the above conservation equations.

2.2 Numerical methods for simulation of the reactive Euler equations

The algorithm for numerically solving the reactive Euler equations is based on Shu and Osher's semi-discrete (method of lines) scheme [8], with Jiang and Shu's weighted essentially non-oscillatory (WENO) interpolation [9]. The details of this method, along with boundary treatment can also be found in [10]. The purpose for picking this algorithm is two-fold. First, by formulating the problem in a semi-discrete manner, spatial and temporal discretization are accomplished independent of one another. This makes the code easy to write for multi-dimensional forced problems. The second reason is that by using high-order spatial and temporal discretization, very accurate solutions are obtainable (formally at least in continuous regions of the flow).

2.3 Numerical solutions to 2-D unsteady detonations

The polytropic EOS can be used as a model of condensed phase explosive provided appropriate values of the EOS parameters are chosen. Also, a rate law that reflects representative detonation time scales and reaction lengths must be given. For the studies in this paper, we take

$$r = H(p - 1\text{GPa})2.5147\,\mu\text{s}^{-1}(1 - \lambda)^{\frac{1}{2}} \quad ,$$

as the rate law (H is the Heaviside function). We also use $Q = 4$ mm$^2/\mu$s^2, $\gamma = 3$ and upstream conditions $p_o = 10^{-4}$ GPa, $\rho_o = 2$ gm/cc and $\vec{u} = 0$. These parameters give $D_{CJ} = 8$ mm/μs, and a steady-state 1-D half-reaction-zone length of 1mm (with a complete reaction-zone length of roughly 4mm.) Each of the following cases were computed with 10 points in the half reaction zone (or 40 points in the complete reaction zone.) Each was also given the same initial conditions, a (numerically) steady CJ detonation traveling to the right with the shock initially located at $x = 8$ mm. The numerical steady traveling wave was computed by placing the exact ZND solution on the grid and allowing it to come to steady state numerically. All shock capturing schemes have some transient initial start-up errors associated with the smearing of the initial shock profile. Using the numerical initial condition was done for the purposes of measuring intrinsic quantities, described later in Section 3.

2.3.1 Expanding channel

The first example examines an initially planar detonation diffraction around a rigid 90° corner. One expects that the detonation front will decelerate as a rarefaction wave is sent through the reaction zone. Figure 1 shows the solution at 6μs as a Schlieren-like plot (i.e. a gray-scale plot of $|\vec{\nabla}\rho|$). (At time $t = 0$, the planar detonation shock is located at $x = 8$mm, in the lower ($y < 35$mm) channel). Figure 1 shows the contact discontinuity (above the vortex at the corner) associated with a change in the temperature of the shocked material near the corner. This also corresponds to a lower shock pressure, and thus to a detonation front traveling below the CJ speed. Also, notice that it takes a finite time for the shock front (near the bottom wall) to sense the effects of the rarefaction wave. This is clearly shown in the Schlieren plot.

2.3.2 Converging channel

This second example focuses on the converging dynamics of detonation. Here, a planar-CJ detonation encounters a rigid 20° ramp. The detonation shock initially forms a Mach reflection which slowly changes to a weaker compressive wave. Now, the front speed is increased above the CJ value in the Mach-stem area. Figure 2 shows the Schlieren gray-scale image at 7μs (At time $t = 0$, the planar detonation shock is located at $x = 8$mm, in the channel). The reflected shock wave can be seen clearly, but note that the Mach stem is curved as was observed in [15].

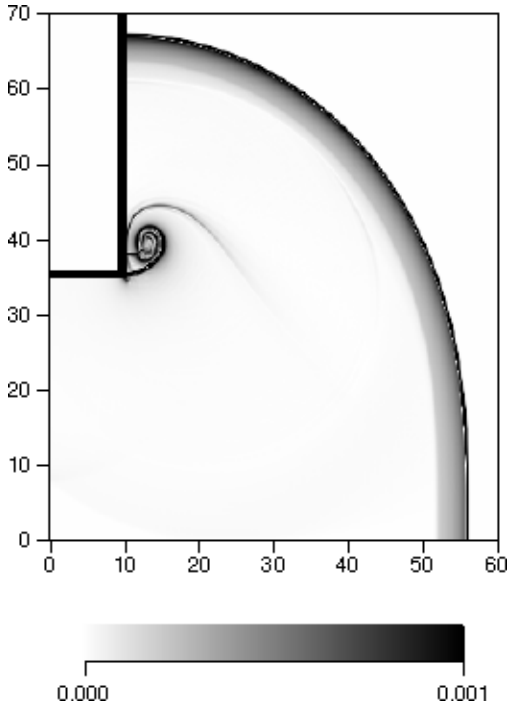

Figure 1: Schlieren-like gray-scale plot of $|\vec{\nabla}\rho| - [gm/mm^4]$ at 6μs, as computed by the fifth-order WENO scheme.

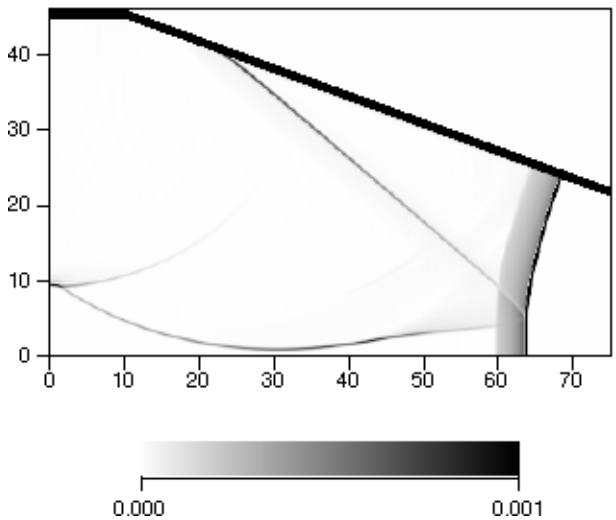

Figure 2: Schlieren-like gray-scale plot of $|\vec{\nabla}\rho| - [gm/mm^4]$ at 7μs, as computed by the fifth-order WENO scheme.

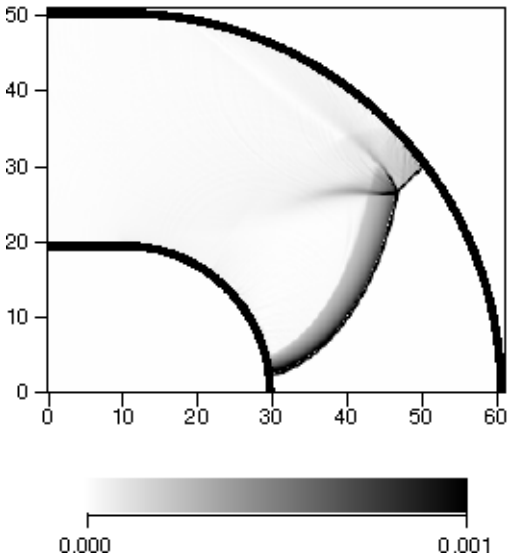

Figure 3: Schlieren-like gray-scale plot of $|\vec{\nabla}\rho| - [gm/mm^4]$ at 5μs, as computed by the fifth-order WENO scheme.

2.3.3 Circular arc

The final example combines both converging and diverging aspects of detonation propagation. An initially planar detonation in a channel encounters a circular bend. The bend has an inner radius of 20mm and an outer radius of 50mm. See Figure 3. A rarefaction wave is initially generated at the inner bend, while a compressive wave is generated from the outer bend. These each influence the shape of the propagating detonation front. At about 3μs after the detonation front encounters the bend, the compressive wave and rarefaction wave collide; eventually the front becomes kinked and forms a Mach reflection as shown in Figure 3.

3 Measuring intrinsic properties of the detonation shock front

One way of comparing DSD with a DNS is to simply look at the motion of the shock fronts generated by both solutions. This will be the approach in this work. Another method would be to suppose there exists an intrinsic relation that governs a detonation shock front, and try to measure this relation directly from a DNS.

As stated previously, one can directly measure the dynamics of the detonation front by solving the compressible, reactive Euler equations with a

DNS. Unfortunately, intrinsic shock-front information like the detonation shock speed, curvature of the shock front, etc. are not directly available from a DNS. But, since the fluid under goes a very strong shock (the Mach number of the shock is about 650), for this detonation model, the density jump at the shock is roughly a constant. So the detonation front may be approximated as the locus of positions of the first occurence of an intermediate density (3gm/cc was used in these computations), between the undisturbed density (2gm/cc) and the shocked density (4gm/cc). And for problems with quiescent upstream conditions, the detonation shock front will pass a fixed Eulerian point at most only once.

Thus, it is possible to create a DNS burn table by sweeping over the computational grid and searching for grid points where the quantity $(\rho - 3\text{gm/cc})$ changes sign from one time level to the next. The first such occurrence will be when the shock passes over that fixed Eulerian point. Then, linear interpolation in time is used to get an accurate estimate of the burn time, $t_b^{\text{DNS}}(x, y)$. Once we have this DNS burn table, important quantities such as shock speed, curvature, etc. may be found. For example, the shock speed is given by $D_n = 1/|\vec{\nabla} t_b|$. The front locations are given simply as contours of $t_b^{\text{DNS}}(x, y)$. The contours of the DNS burn times and instantaneous detonation velocities for the three previous examples are shown in Section 5. Next, we discuss the various functional forms of the intrinsic PDE's.

4 Intrinsic partial differential equations from detonation shock dynamics

4.1 Huygens' Construction

The Huygens' construction assumes the detonation normal velocity is equal to the Chapman-Jouget velocity, i.e. $D_n = D_{CJ} = 8\text{mm}/\mu\text{s}$, for our example. Numerically, this is solved using the level set algorithm presented in [5] and [6]. In particular, the level set of a field function, ψ, is used to describe the motion of the detonation shock, and the evolution of ψ is given by the level set equation

$$\frac{\partial \psi}{\partial t} + D_{CJ} |\vec{\nabla} \psi| = 0. \tag{3}$$

Second order essentially non-oscillatory (ENO) interpolation is used in calculating spatial derivatives appearing in (3). A forward Euler method is used for the time integration. The boundary conditions at a rigid wall are fairly simple for this model. If the shock wave normal at the boundary points into the inert region, nothing is done. If the shock wave normal at the boundary

points into the explosive region, then it is set be perpendicular to the rigid wall/explosive interface.

4.2 $D_n - \kappa$ relation

A $D_n - \kappa$ relation gives parabolic front evolution, see [7]. Disturbances to the shock front diffuse across the front via parabolic evolution. For this ideal model, the first term of an asymptotic DSD theory [4] gives a linear $D_n(\kappa)$ relation $D_n = 8\text{mm}/\mu\text{s} - 66.8\text{mm}^2/\mu\text{s}\ \kappa$. For comparison to previous results in [6], we use a $D_n(\kappa)$ shown in Figure 4, which corresponds to making a nozzle approximation to the flow, which is assumed to be quasi-steady. Since the $D_n - \kappa$ curve is generated numerically, a polynomial fit is used in these computations. For $\kappa < 0$, the $D_n - \kappa$ relation used is a linear extrapolation from $\kappa > 0$, which gives $D_n = 8\text{mm}/\mu\text{s} - 66.8\text{mm}^2/\mu\text{s}\ \kappa$. The motion of the detonation shock is solved numerically with the level set algorithm presented in [5] and [6]. For this type of intrinsic relation, the following level set equation is solved,

$$\frac{\partial \psi}{\partial t} + D_n(\kappa)|\vec{\nabla}\psi| = 0, \tag{4}$$

where $D_n(\kappa)$ is shown in Figure 4. The discretization is the same as in section 4.1, with the curvature being approximated with second order central differences. For this model, an angle boundary condition is appropriate [6]. For all cases in section 5, it is appropriate to enforce that the shock normal be perpendicular to the rigid wall/explosive interface.

4.3 $\dot{D}_n - D_n - \kappa$ relation

Unlike the $D_n - \kappa$ relation, a $\dot{D}_n - D_n - \kappa$ relation is hyperbolic under certain conditions, see the discussion in [7]. In particular, disturbances will propagate at finite speeds along the shock front. The square root of the ratio of the coefficients multiplying κ and $\dot{D}_n$ determines this transverse signaling speed, see [7].

Disturbances travel at finite speeds along the shock front for the full reactive Euler equations. An infinitesimal disturbance travels outward along the wavefront at a speed equal to the local sound speed plus it will be advected with the local particle speed. A simple analysis of inert strong shock states (for ideal EOS) shows that a disturbance will travel at a speed $[(\gamma - 1)/(\gamma + 1)]^{1/2} D_n$ along the shock, see pg. 249 of [11]. A more detailed analysis including the reaction zone effects has been carried out to see how the transverse signaling speed is changed by a reaction zone structure. For a

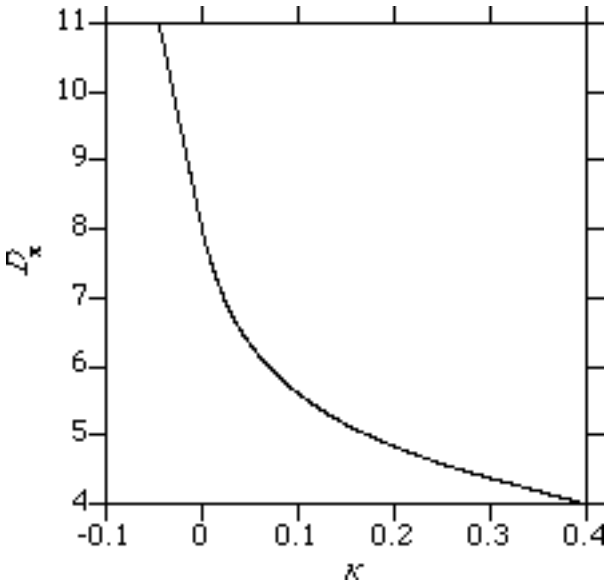

Figure 4: $D_n(\kappa)$ law for ideal equation of state model.

detonation wave, a signal will travel transverse to the shock at a speed equal to the maximum value of $(c^2 - u^2)^{1/2}$ within the reaction zone (here, c is the local sound speed, and u is the local particle speed relative to the shock). For $\gamma > 2$, this value is maximum at the shock, and thus disturbances will travel at a speed equal to the inert case, $[(\gamma - 1)/(\gamma + 1)]^{1/2} D_n$. For $\gamma < 2$, there is an interior point in the reaction zone which has a maximum value of $(c^2 - u^2)^{1/2}$. In this case, the disturbance will travel faster than the inert shock case. For $\gamma = 3$, the transverse propagation speed of a disturbance will travel at $D_n/2^{1/2}$.

The theory of Yao and Stewart [12] derives a $\dot{D}_n - D_n - \kappa$ relation which can not be written as $\dot{D}_n(D_n, \kappa)$, since $\dot{D}_n$ is not defined for certain regions of (D_n, κ) space, and is multi-valued for others [12]. So, instead a functional form of the $\dot{D}_n - D_n - \kappa$ relation was chosen as a model to give the steady $D_n(\kappa)$ relation of Section 4.2 when $\dot{D}_n = 0$. The rest of the $\dot{D}_n - D_n - \kappa$ function was determined by setting the transverse signaling speed of the $\dot{D}_n - D_n - \kappa$ relation to be that of the full reactive Euler equations. This gives the following $\dot{D}_n - D_n - \kappa$ relation for $\gamma = 3$:

$$\dot{D}_n(D_n, \kappa) = -\frac{1}{2} D_n^2 \kappa + \beta(D_n) \tag{5}$$

where

$$\beta(D_n) = \begin{cases} 3.832(\ln(8) - \ln(D_n))(1 + .145(8 - D_n)^{1/4}), & \text{if } D_n < 8 \\ .007485 D_n^2 (8 - D_n), & \text{if } D_n \geq 8. \end{cases}$$

Note that this $\dot{D}_n - D_n - \kappa$ relation was not derived, but rather empirically determined. We note that Brun et al [16] had used a similar model for transient detonation waves. A contour plot of the above relation is shown in Figure 5. Notice that the contour $\dot{D}_n = 0$ gives essentially the steady $D_n - \kappa$ relation of Figure 4. Since the normal acceleration of the front is needed, the level set PDE will need to be modified to reflect this type of relation. The equation for the level-set function, ψ, is basically unchanged from (4)

$$\frac{\partial \psi}{\partial t} + D_n |\vec{\nabla}\psi| = 0, \tag{6}$$

except that the velocity, D_n, is now a variable and the total derivative of D_n is governed by

$$\frac{D(D_n)}{Dt} = \frac{\partial D_n}{\partial t} + D_n \hat{n} \cdot \vec{\nabla} D_n = \dot{D}_n(D_n, \kappa), \tag{7}$$

where $\hat{n}$ is the shock front normal, $\hat{n} = \vec{\nabla}\psi / |\vec{\nabla}\psi|$, $\frac{D(D_n)}{Dt}$ is the total derivative of D_n, and $\dot{D}_n(D_n, \kappa)$ is given from equation (5) for this model. These equations form a coupled set of nonlinear PDEs for the evolution of the level-set function and its normal velocity. These equations (6) and (7) along with equation (5) can be cast in the following conservative form:

$$(\vec{\nabla}\psi)_t + \vec{\nabla}(D_n |\vec{\nabla}\psi|) = 0 \tag{8}$$

$$(D_n)_t + \vec{\nabla} \cdot (\frac{D_n^2 \vec{\nabla}\psi}{2|\vec{\nabla}\psi|}) = \beta(D_n) \tag{9}$$

These two equations form a nonlinear conservative hyperbolic system. In particular, we expect jumps in the gradient of the level set function, and jumps in the detonation velocity at discontinuities. This would give a kink in the shock locus associated with a jump in the detonation velocity. This system of equations has not been investigated elsewhere, to the best of our knowledge. We present the jump conditions associated with the above system of equations (8) and (9) in section 4.3.2. But first, it should be noted that Whitham's geometrical shock dynamics [11] model for propagating inert shocks is also a $\dot{D}_n - D_n - \kappa$ relation. Next, we briefly discuss Whitham's equations and how they are solved in [11].

4.3.1 Whitham's Geometrical Shock Dynamics

Whitham's geometrical shock dynamics equations [11] may be interpreted as a $\dot{D}_n - D_n - \kappa$ relation (here D_n is the Mach number of the shock wave, and

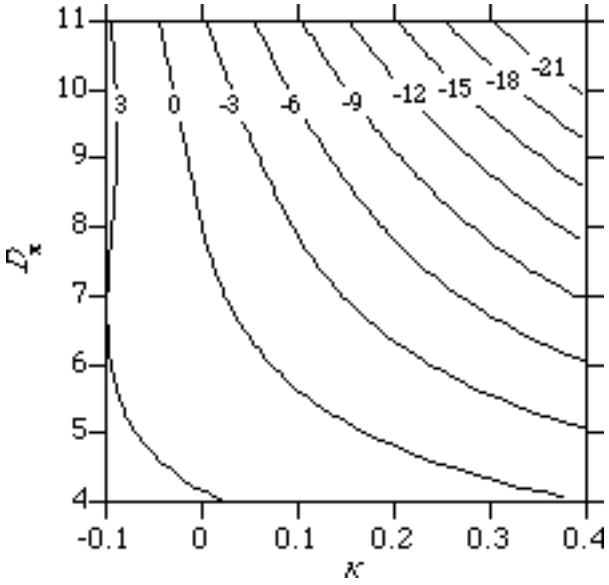

Figure 5: $\dot{D}_n - D_n - \kappa$ relation for ideal equation of state model. Contours correspond to constant values of $\dot{D}_n$.

$\dot{D}_n$ is the shock acceleration in the normal direction). The relation is given by

$$\dot{D}_n = -\frac{(D_n^2 - 1)}{\lambda(D_n)}\kappa \tag{10}$$

where

$$\lambda(D_n) = \left(1 + \frac{2}{\gamma + 1}\frac{1 - \mu^2}{\mu}\right)\left(1 + 2\mu + \frac{1}{D_n^2}\right)$$

and

$$\mu^2 = \frac{(\gamma - 1)D_n^2 + 2}{2\gamma D_n^2 - (\gamma - 1)}.$$

Whitham formulated a PDE for his $\dot{D}_n - D_n - \kappa$ relation in terms of a shock arrival time function, $\alpha(\vec{x})$. His formulae are:

$$D_n = \frac{1}{|\vec{\nabla}\alpha|} \tag{11}$$

$$\vec{\nabla} \cdot (\frac{D_n}{A}\vec{\nabla}\alpha) = 0 \tag{12}$$

where D_n is the Mach number of the shock wave and $A(D_n)$ is the Mach number area rule. The shock locus at any particular time is given by the equation $\alpha(\vec{x}) = t$. Since Whitham's model is also a system of nonlinear

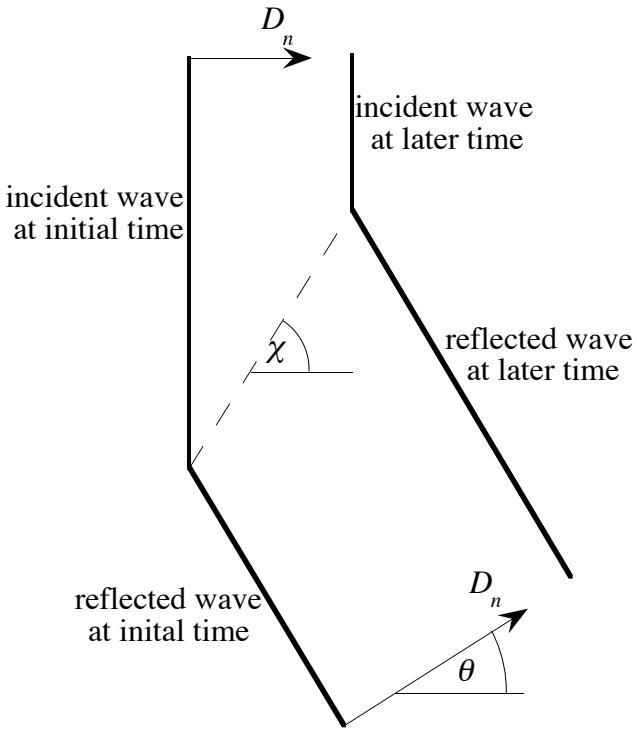

Figure 6: Schematic for defining deflection angle, θ, and shock-shock reflection angle, $\chi - \theta$, after Whitham [11].

hyperbolic conservation equations, it too will have the possibility of forming discontinuities (kinks in the shock locus, associated with jumps in the normal velocity). We will express our jump conditions in a similar manner. In particular, for Whitham's equations, there is a relation (at least for strong shocks) between the deflection angle, θ, at a kink and the shock-shock reflection angle, $\chi - \theta$. See figure 6. See pg. 299 of [11] to see a plot of $\chi - \theta$ versus θ for Whitham's geometrical shock dynamics, with $\gamma = 1.4$.

4.3.2 Jump conditions for $\dot{D}_n - D_n - \kappa$ relations

We can recover a Whitham-like formulation by making the following substitutions:

$$\psi(\vec{x}, t) \rightarrow \alpha(\vec{x}, t) - t \tag{13}$$

and

$$D_n(\vec{x}, t) \rightarrow D_n(\vec{x}) \tag{14}$$

in the equations (8) and (9), which yields:

$$\vec{\nabla}(D_n|\vec{\nabla}\alpha|) = 0 \tag{15}$$

$$\vec{\nabla}\cdot(\frac{D_n^2\vec{\nabla}\alpha}{2|\vec{\nabla}\alpha|}) = \beta(D_n) \tag{16}$$

Note that equation (15) states that $D_n|\vec{\nabla}\psi|$ is a constant, and equation (6) specifies the constant to be one:

$$D_n|\vec{\nabla}\psi| = 1,$$

which yields precisely equation (11). Substituting this into (16), and taking $A(D_n) = 2/D_n^2$ yields equation (12) with the addition of the source-like function $\beta(D_n)$ on the right hand side:

$$\vec{\nabla}\cdot(\frac{D_n\vec{\nabla}\alpha}{A}) = \beta(D_n). \tag{17}$$

We can then apply the divergence theorem to equation (17) to obtain the jump conditions. The source term, $\beta(D_n)$, plays no role in the jump conditions, since it is an O(1) quantity, and we can take a small enough "box" around the discontinuity to eliminate its role. Not surprisingly, the jump conditions can be expressed in terms of the shock deflection angle, θ, and the shock-shock spreading angle, $\chi - \theta$, defined in figure 6. These are related as follows:

$$\sin(\chi) + \frac{\cos^2(\chi-\theta)}{\cos^2(\chi)}\sin(\chi-\theta) = 0. \tag{18}$$

A plot of this relation is shown in figure 7. In particular, when the deflection angle, θ, is small, we see that $\chi - \theta = \tan^{-1}(1/\sqrt{2})$. This corresponds to a very weak, acoustic-like, reflected wave. As the deflection angle is increased, the shock-shock spreading angle decreases. This would physically correspond to a Mach reflection, and as the deflection angle is increased to 90°, the spreading angle tends toward zero. Of coarse for the full Euler equations, there comes a point when this Mach reflection transits to a regular reflection. This is not the case for both the model here and Whitham's geometrical shock dynamics.

Although equation (17) is a perfectly valid PDE, this formulation is typically more difficult to solve general problems. The level set formulation, equations (8) and (9), are typically more convenient. One can use standard shock capturing schemes to discretize the conservative hyperbolic PDEs. Of concern is whether the extra independent variable (time in this case) will play a role in the jump conditions. In particular, does the embedding of the level curves near a discontinuity affect the jump conditions? Clearly there

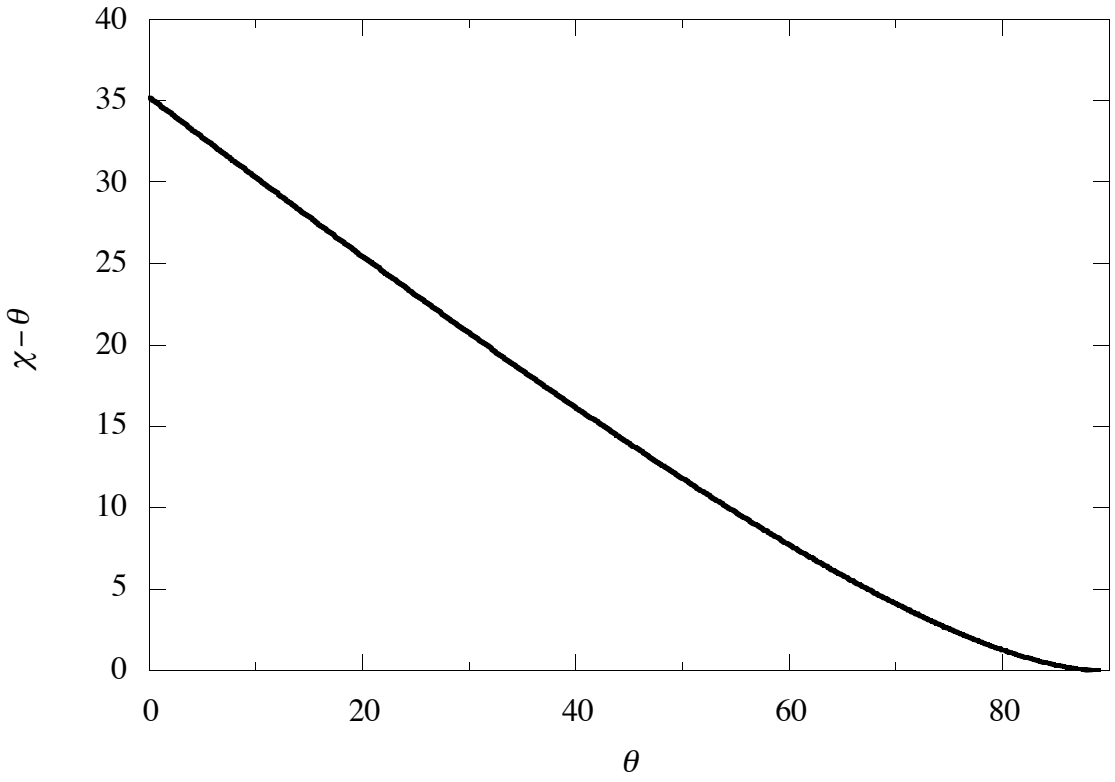

Figure 7: Shock-shock reflection angle, $\chi - \theta$, versus shock deflection angle, θ, for the Whitham-like formulation expressed in equation (17).

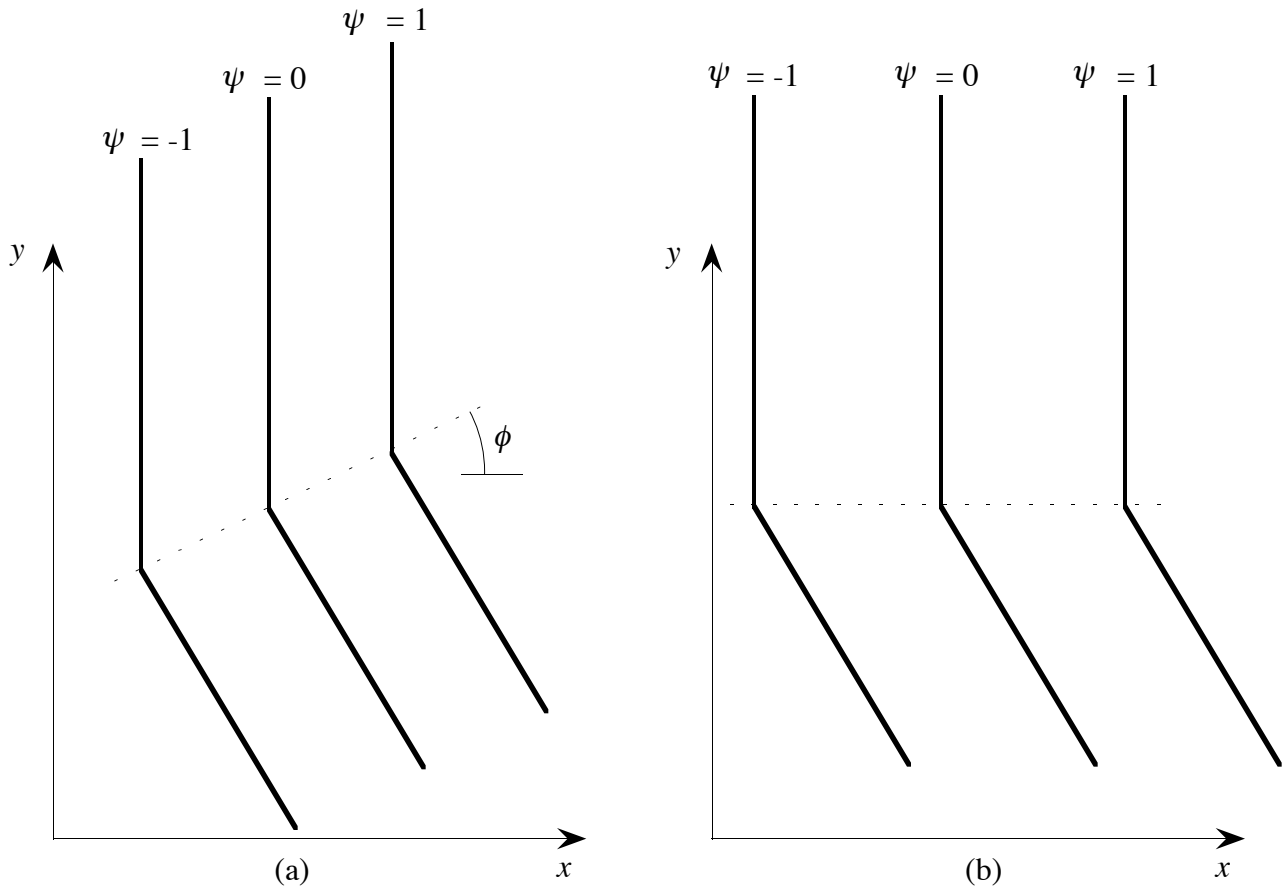

Figure 8: Two possible embeddings of the initial wave shape in figure 6.

are an infinite number of different ways to embed a curve with a kink. See figure 8 for two possible embeddings of the initial wave in figure 6. In both cases (a) and (b), the location and velocity of the $\psi = 0$ curve are the same. The difference is that the other level curves are in different locations. In particular, the level set function, ψ has a discontinuity locus that is different for embedding (a) and (b). The discontinuity locus makes an angle ϕ above the x-axis. One would hope that this embedding does not play a role in the solution to the intrinsic PDEs (this is the case for a Huygens' construction and the $D_n - \kappa$ relation, see [6].) Next, we explore the jump conditions of the level set equations (8) and (9).

Again, one can use the divergence theorem on equations (8) and (9) to obtain jump conditions. The major difference is that the level set formulation has one extra independent variable, namely time. The other difference is that the embedding angle, ϕ, also plays a role in the integration that results from the divergence theorem. It is more convenient to define the angle ω between

the shock-shock trajectory, χ and the embedded angle, ϕ. This is given by $\omega = \chi - \phi$. The resulting jump conditions can be cast in terms of the angles ω, χ and θ as:

$$\frac{-2\sin(\omega)}{\cos(\chi)}(1-\frac{\cos(\chi-\theta)}{\cos(\chi)})-\sin(\chi-\omega)+\frac{\cos^2(\chi-\theta)}{\cos^2(\chi)}\sin(\chi-\theta-\omega)=0 \quad (19)$$

It can easily be seen that if the angle ω is zero, then the jump conditions are the same as equation (18). But, if ω is non-zero, then different jump conditions can exist. This indicates that a particular level curve will have a jump condition that can be influenced by the surrounding level curves. This is clearly not desirable, since the evolution of a particular level curve can depend on how it is embedded. Figure 9 indicates the range of possible jump conditions given by equation (19). Notice that the $\omega = 0$ curve is precisely the curve given in figure 7. Also notice that for θ small, the possible differences are small. Only at large deflection angles, θ, and large ω does one see significant differences. Also, one might be able to solve the time-dependent level set equations to steady state, and thus the ω dependence would not play a role, and the Whitham-like jump conditions would be recovered.

4.3.3 Numerical formulation for $\dot{D}_n - D_n - \kappa$ relations

Here, we use the level set formulation, equations (8) and (9), expressed in two dimensional Cartesian coordinates, namely:

$$(u)_t + (D_n(u^2+v^2)^{1/2})_x = 0 \quad ,$$

$$(v)_t + (D_n(u^2+v^2)^{1/2})_y = 0 \quad ,$$

$$(D_n)_t + (\frac{D_n^2 u}{2(u^2+v^2)^{1/2}})_x + (\frac{D_n^2 v}{2(u^2+v^2)^{1/2}})_y = \beta(D_n), \quad (20)$$

where $u = \psi_x$, and $v = \psi_y$. These equations are solved numerically using the Lax-Freidrichs algorithm with third order WENO interpolation described in [10]. We also integrate the level set equation (6) using u, v and D_n from equation (20), to evaluate the second term in the level set equation (6). This is necessary in finding the location of the front and its' detonation velocity. As with the $D_n - \kappa$ relation, the shock normal at the rigid wall is forced to be perpendicular to the wall. Next, the detonation front dynamics generated from the DNS are compared with those from the three intrinsic relationships.

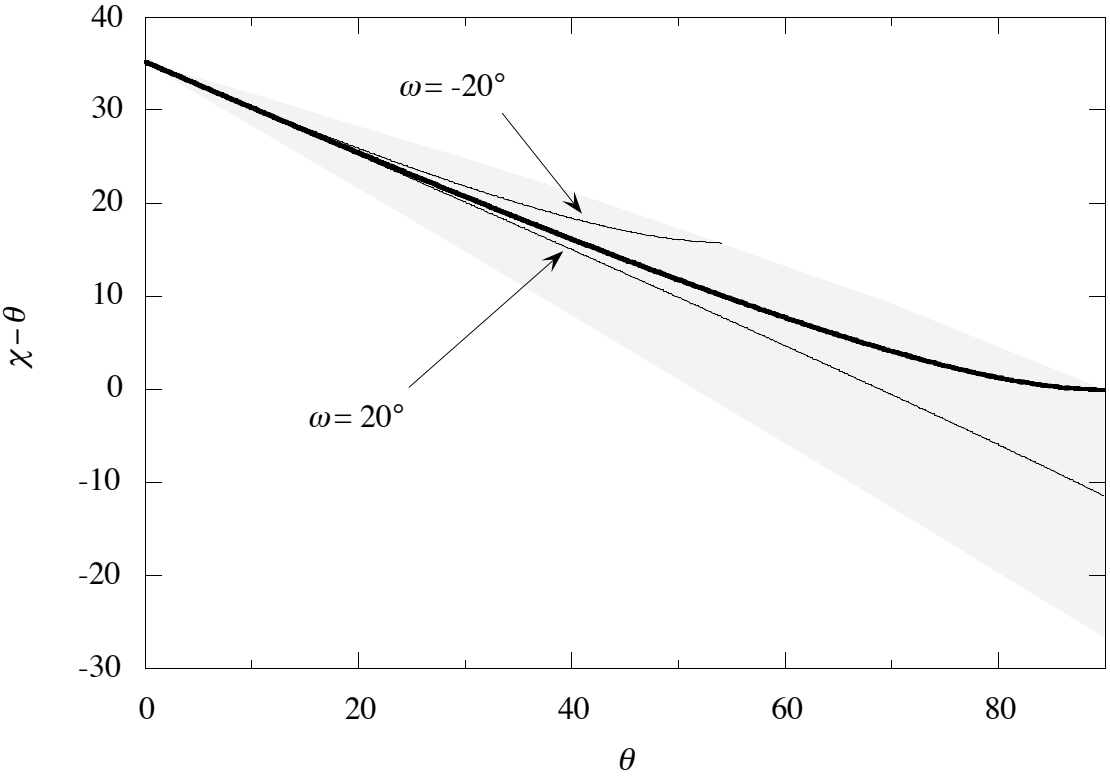

Figure 9: Shock-shock reflection angle, $\chi - \theta$, versus shock deflection angle, θ, for various embedding angles, ω. The gray region denotes all physically realizable solutions. The dark line indicates the $\omega = 0$ solution.

5 Examples and comparisons

Here, comparisons between direct numerical simulation of detonation, and level-set solutions to three intrinsic PDEs are made. The three intrinsic relations are: the Huygens' construction, a $D_n - \kappa$ relation and a $\dot{D}_n - D_n - \kappa$ relation. For the Huygens' solution and the $D_n - \kappa$ solution, we computed the solutions with $\Delta x = 0.2$mm. For the $\dot{D}_n - D_n - \kappa$ simulations, we used $\Delta x = 0.1$mm. The finer grid for the $\dot{D}_n - D_n - \kappa$ relation was used since its' solution is very close to the DNS (this eliminated small errors in mapping from the DSD grid to the DNS grid.) A self-convergence study was performed on the numerical solutions to the DSD intrinsic relations and to the DNS. The study indicates that shock arrival solutions presented here are in error at most $\pm 0.05\mu$s (usually much less).

5.1 Expanding channel

The measuring technique described in Section 3 is used to calculate the front locations and Eulerian records of the detonation velocity, D_n, from the DNS for the expanding channel problem. These records are displayed in Figure 10. The detonation velocity is clearly seen to decrease by roughly 50% from the D_{CJ} value of 8mm/μs. Also, notice that the signaling speed is clearly evident in the simulation, and matches the correct speed given from acoustic theory [11].

The Huygens' solution is given in Figure 11. The dashed lines represent the fronts from the Huygens' solution, while the DNS fronts from Figure 10 are given as solid lines for comparison. Notice that there is a large discrepancy in the shapes and velocities of the fronts.

The $D_n - \kappa$ solution is given in Figure 12. The detonation front slows as the front goes around the corner. Also, since the underlying PDE is parabolic, the entire front instantaneously senses disturbances at the front, as seen by the gray-scale plot of the normal velocity. Although this is not physically correct, the dynamics of a $D_n - \kappa$ do predict velocity deficits, which were seen in the DNS.

The $\dot{D}_n - D_n - \kappa$ solution is given in Figure 13. Notice that the disturbances propagate at a finite speed from the corner, as predicted in Section 4.3. Notice also that for this problem the shapes and resulting detonation velocities compare well with the DNS.

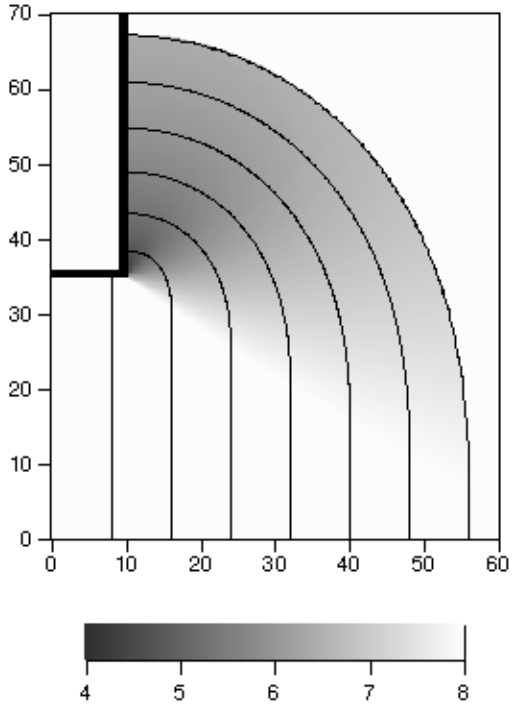

Figure 10: Fronts at intervals of 1μs are shown as solid lines, and the detonation normal velocities [mm/μs] calculated from the DNS are given as the gray scale.

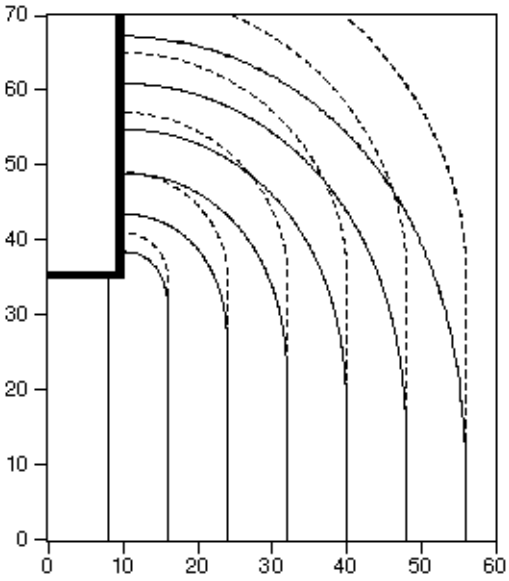

Figure 11: Fronts at intervals of 1μs are shown as solid lines from the DNS, and as dotted lines from the Huygens' solution.

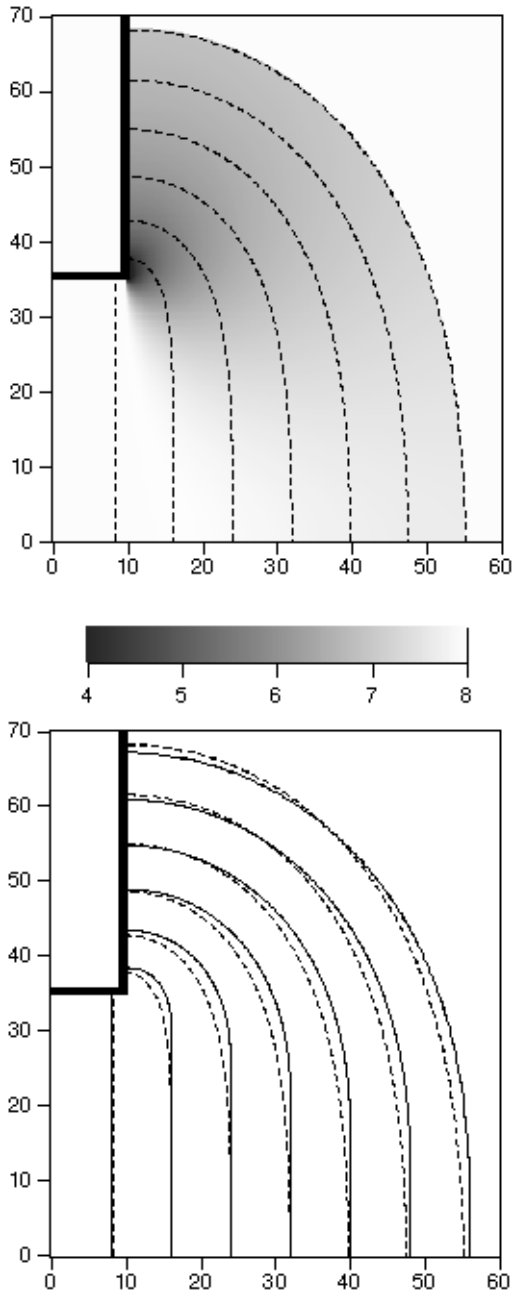

Figure 12: The top figure shows the fronts at intervals of 1μs, and detonation velocities [mm/μs] as calculated from the level-set $D_n - \kappa$ solution. Fronts are shown as solid lines from the DNS, and as dotted lines from the $D_n - \kappa$ solution in the bottom figure.

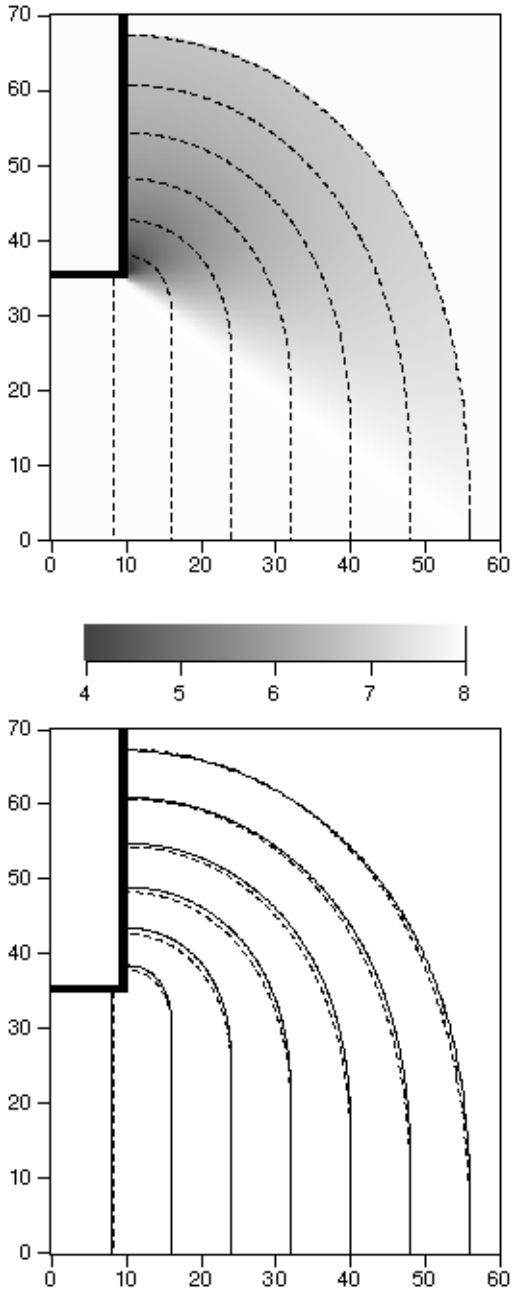

Figure 13: The top figure shows the fronts at intervals of 1μs, and detonation velocities [mm/μs] as calculated from the level-set $\dot{D}_n - D_n - \kappa$ solution. Fronts are shown as solid lines from the DNS, and as dotted lines from the $\dot{D}_n - D_n - \kappa$ solution in the bottom figure.

5.2 Converging channel

The measuring technique described in Section 3 is again used to calculate the front locations and Eulerian records of the detonation velocity, D_n, from the DNS for the converging channel problem. These records are displayed in Figure 14. The detonation velocity is clearly seen to increase to about 9.5mm/μs from the CJ value of 8mm/μs. Also, notice that the disturbance from the wedge travels at a finite speed into the steady one-dimensional detonation region.

The Huygens' solution is given in Figure 15. The dashed lines represent the fronts from the Huygens' solution, while the DNS fronts from Figure 14 are given as solid lines for comparison. Notice that the Huygens' solution is just a flat wave solution, and no shape changes are predicted.

The $D_n - \kappa$ solution is given in Figure 16. The detonation front increases in speed as the front changes angle at the upper boundary to satisfy the reflection boundary condition. Since the underlying PDE is parabolic, the entire front instantaneously senses disturbances at the front, as seen by the gray-scale plot of the normal velocity. Again, this is not physically correct, but the $D_n - \kappa$ solution does predict a velocity increase.

The $\dot{D}_n - D_n - \kappa$ solution is given in Figure 17. Notice that the disturbances propagate at a finite speed from the ramp. Also notice that there is initially a kink in the wave front, associated with a shock–shock-like reflection from the ramp. This solution, unlike Whitham's Geometrical Shock Dynamics model for inerts, is not self-similar. The detonation velocity is actually decreasing along the ramp wall as a function of time. This is due to the $\beta(D_n)$ forcing term in the $\dot{D}_n - D_n - \kappa$ relation. Notice also that for this problem the shapes and resulting detonation velocities compare well with the DNS. Even though the acoustic transverse propagation speed is exactly the same as for the full compressible Euler equations, the triple point tracks are slightly different. This is due to the fact that the jump conditions for the intrinsic PDE are different than the Euler equations. For this problem, it is interesting to note how the embedding angle changes the jump condition from that of a Whitham formulation. For this case the embedding angle, ϕ, is 20°. The deflection angle, θ is also 20°. From the jump conditions, we have $\omega = 25.16°$ and $\chi - \theta = 25.16°$. This is very close to θ and χ as the Whitham formulation would be ($\omega = 0$), with $\theta = 20°$, and $\chi - \theta = 25.48°$. The relative difference in shock-shock deflection angle is only about 1%.

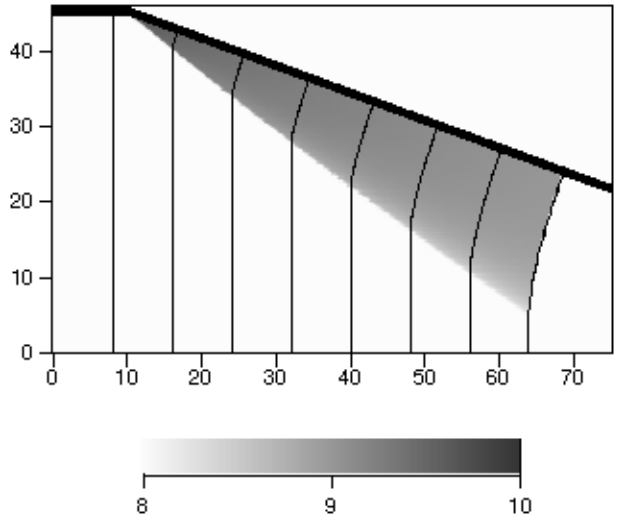

Figure 14: Fronts at intervals of 1μs are shown as solid lines, and the detonation normal velocities [mm/μs] calculated from the DNS are given as the gray scale.

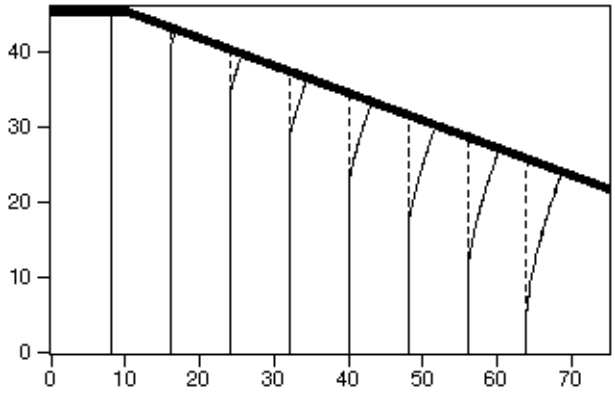

Figure 15: Fronts at intervals of 1μs are shown as solid lines from the DNS, and as dotted lines from the Huygens' solution.

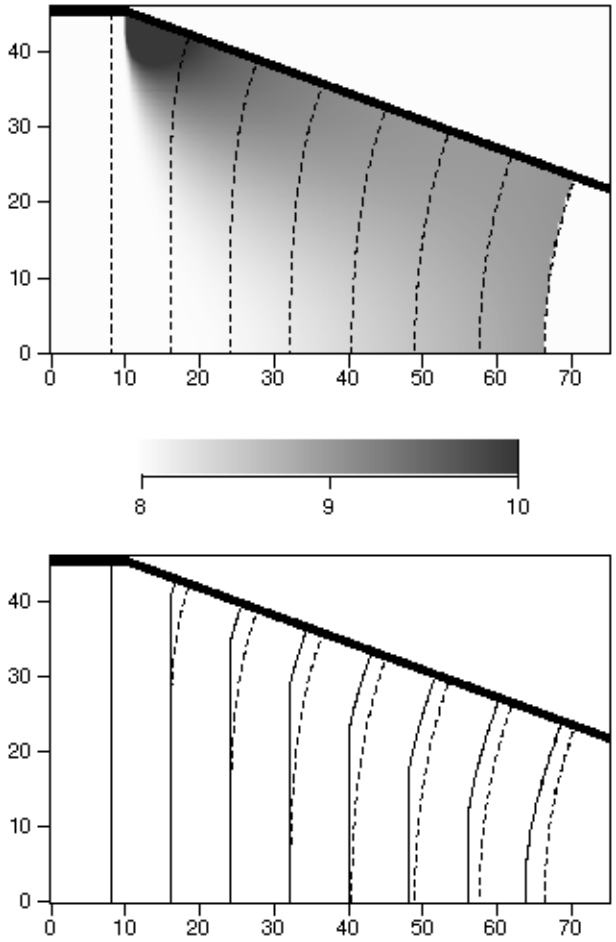

Figure 16: The top figure shows the fronts at intervals of 1μs, and detonation velocities [mm/μs] as calculated from the level-set $D_n - \kappa$ solution. Fronts are shown as solid lines from the DNS, and as dotted lines from the $D_n - \kappa$ solution in the bottom figure.

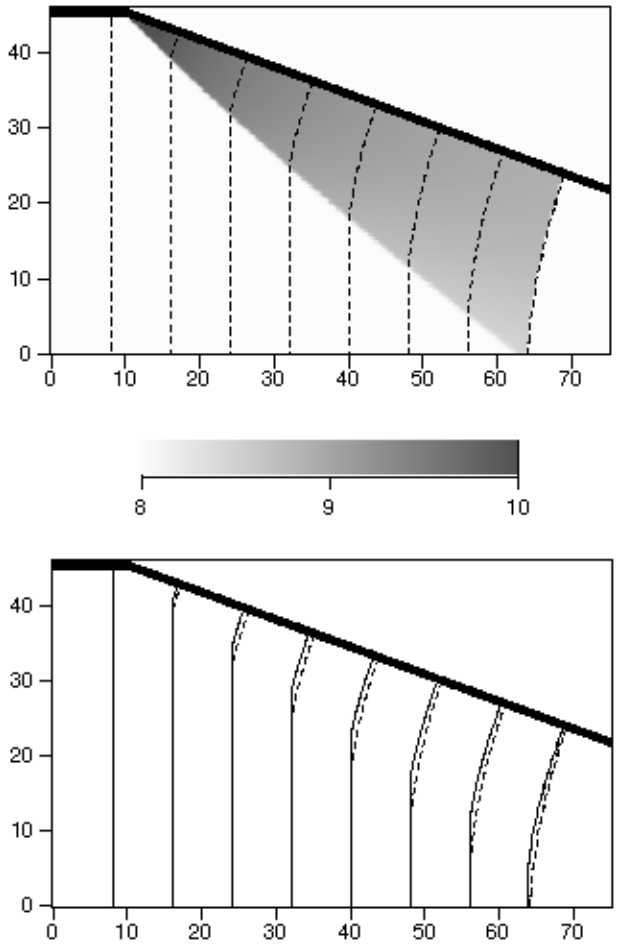

Figure 17: The top figure shows the fronts at intervals of 1μs, and detonation velocities [mm/μs] as calculated from the level-set $\dot{D}_n - D_n - \kappa$ solution. Fronts are shown as solid lines from the DNS, and as dotted lines from the $\dot{D}_n - D_n - \kappa$ solution in the bottom figure.

5.3 Circular arc

Again the measuring technique described in Section 3 is used to calculate the front locations and Eulerian records of the detonation velocity, D_n, from the DNS for the circular arc problem. These records are displayed in Figure 18. The detonation velocity is clearly seen to increase along the outer bend, where the detonation senses a compressive wave, and is far below D_{CJ} along the inner bend, where there is a rarefaction wave, and the detonation diverges. Also, notice that the disturbance from the edges can be seen to travel at a finite speed into the steady one-dimensional detonation region.

The Huygens' solution is given in Figure 19. The dashed lines represent the fronts from the Huygens' solution, while the DNS fronts from Figure 18 are given as solid lines for comparison. Notice that the Huygens' solution predicts a flat wave along the top of the circular arc, and diffracts around the inner radius of the arc without any decrease in speed. Notice that the general shapes and locations are quite different than the DNS.

The $D_n - \kappa$ solution is given in Figure 20. The detonation front increases in speed along the upper boundary to satisfy the reflection boundary condition, and decreases along the inner radius. Also, the fronts become steady in a frame rotating with the arc very quickly, again this can be attributed to parabolic nature of the $D_n - \kappa$ relation. Although this relation does not predict the shapes very well, the fronts seem to be on average in roughly the right locations.

The $\dot{D}_n - D_n - \kappa$ solution is given in Figure 21. Notice that the disturbances propagate at a finite speed from the inner and outer bends. Also notice that there is a kink that eventually forms, when the compressive wave from the outer radius breaks and forms a shock–shock interaction. Notice also that for this problem the shapes and resulting detonation velocities compare well with the DNS.

Notice also that these three problems are very difficult tests, since the velocities vary far from D_{CJ}, and the curvatures, and time dependence are relatively large.

6 Conclusions

From the examples given here, it seems clear that a $\dot{D}_n - D_n - \kappa$ relation does an excellent job of reproducing the front evolution of a resolved DNS. It alleviates some of the short comings of a $D_n - \kappa$ relation. In particular, since a $\dot{D}_n - D_n - \kappa$ relation is hyperbolic, and signaling speeds can be made finite and are similar to the full reactive Euler equations, the range of influence of disturbances are predicted better than a $D_n - \kappa$ relation.

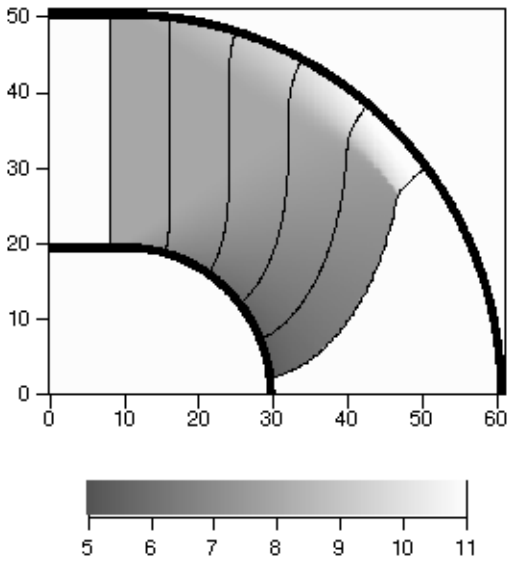

Figure 18: Fronts at intervals of 1 μs are shown as solid lines, and the detonation normal velocities [mm/μs] calculated from the DNS are given as the gray scale.

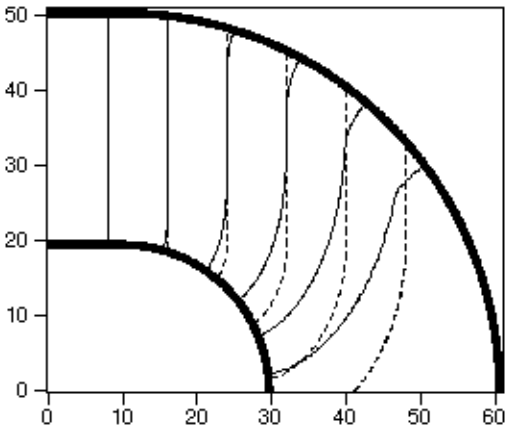

Figure 19: Fronts at intervals of 1 μs are shown as solid lines from the DNS, and as dotted lines from the Huygens' solution.

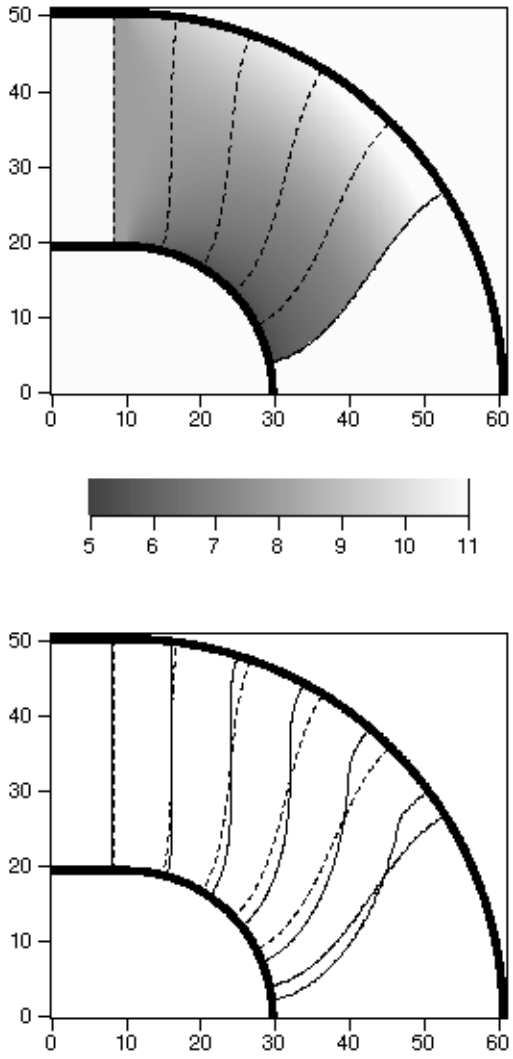

Figure 20: The top figure shows the fronts at intervals of 1 μs, and detonation velocities [mm/μs] as calculated from the level-set $D_n - \kappa$ solution. Fronts are shown as solid lines from the DNS, and as dotted lines from the $D_n - \kappa$ solution in the bottom figure.

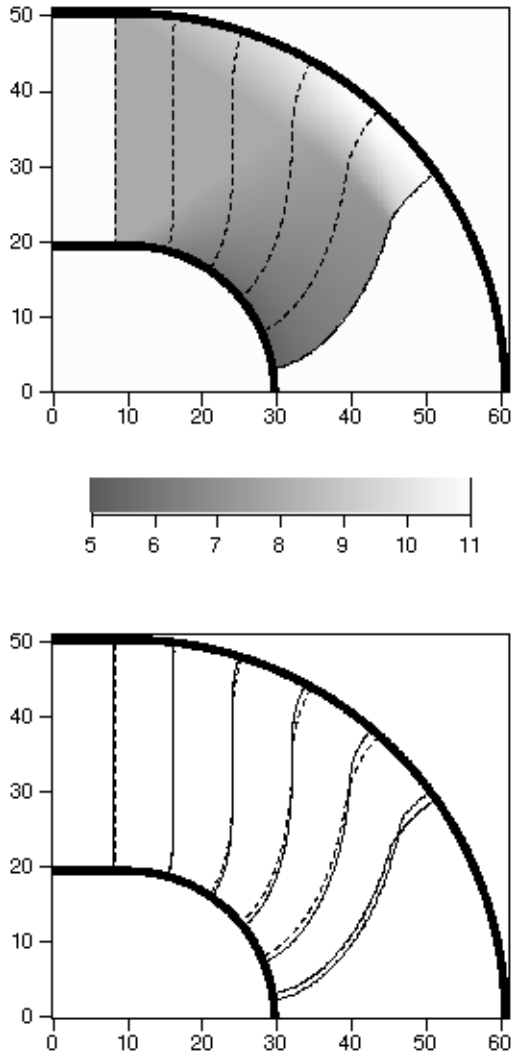

Figure 21: The top figure shows the fronts at intervals of 1 μs, and detonation velocities [mm/μs] as calculated from the level-set $\dot{D}_n - D_n - \kappa$ solution. Fronts are shown as solid lines from the DNS, and as dotted lines from the $\dot{D}_n - D_n - \kappa$ solution in the bottom figure.

Acknowledgments

T. D. Aslam and D. S. Stewart have been supported by the United States Air Force (USAF), Wright Laboratory, Armament Directorate, Eglin Air Force Base, F08630-95-1-0004. Tariq Aslam has also been supported by the U.S. Department of Energy.

References

[1] Chapman, D. L., "On the rate of explosion in gases," *Philosophical Magazine*, 47, 90-104 (1899).

[2] Jouguet, E., "On the propagation of chemical reactions in gases," *Journal de Mathematiques Pures et Appliquees*, 1, 347-425 and 2, 5-85 (1906).

[3] Wood, W. W., and Kirkwood, J. G., "Diameter effect in condensed explosives. The relation between velocity and radius of curvature in the detonation wave," *Journal of Chemical Physics*, 22, 1920-1924 (1954).

[4] Stewart, D. S. and Bdzil, J. B., "The shock dynamics of stable multidimensional detonation," *Combustion and Flame*, 72, 311-323 (1988).

[5] Osher, Stanley and Sethian, James A., "Fronts Propagating with Curvature- Dependent Speed: Algorithms Based on Hamilton-Jacobi Formulations," *Journal of Computational Physics*, 79, 12-49 (1988).

[6] Aslam, Tariq D., Bdzil, John B., and Stewart, D. Scott, "Level Set Methods Applied to Modeling Detonation Shock Dynamics," *Journal of Computational Physics*, 126, 390-409 (1996).

[7] Aslam, Tariq D., "Investigations on Detonation Shock Dynamics," PhD Thesis, University of Illinois at Urbana-Champaign, (1996).

[8] Shu, Chi-Wang and Osher, Stanley, "Efficient Implementation of Essentially Non-oscillatory Shock-Capturing Schemes II," *Journal of Computational Physics*, 83, 32-78 (1989).

[9] Jiang, Guang-Shan and Shu, Chi-Wang, "Efficient Implementation of Weighted ENO Schemes," *Journal of Computational Physics*, 126, 202-228, (1996).

[10] Xu, Shaojie, Aslam, Tariq, and Stewart, D. Scott, "High Resolution Numerical Simulation of Ideal and Non-ideal Compressible Reacting Flows with Embedded Internal Boundaries," *Combustion Theory and Modelling*, Vol 1, Nu 1, 113-142 (1997).

[11] Whitham, G. B., *Linear and Nonlinear Waves*, Wiley (New York) (1974).

[12] Yao, Jin and Stewart, D. Scott, "On the dynamics of multi-dimensional detonation," *Journal of Fluid Mechanics*, 309, 225-275 (1996)

[13] Bdzil, J. B. and Stewart, D. S., "Modeling Two-Dimensional Detonation with Detonation Shock Dynamics," Phys. Fluids A, 1,1261-1267 (1989).

[14] Stewart, D. S., and Bdzil, J. B., "A lecture on detonation shock dynamics," in *Mathematical Modeling in Combustion Science, Lecture Notes in Physics*, 299, 17-30, Springer-Verlag (New York) (1988).

[15] Bdzil, J., Aslam, T., and Stewart, D. S., "Curved Detonation Fronts in Solid Explosives: Collisions and Boundary Interactions," 20th International Symposium on Shock Waves, Pasadena, CA, July 24-28 (1995).

[16] Brun, L., Kneib, J.-M., and Lascaux, P., "Computing the transient self-sustained detonation after a new model," 11th International Detonation Symposium, Boston, MA, July 12-16 (1993).